



Predicting photovoltaic efficiency in Cs-based perovskite solar cells: A comprehensive study integrating SCAPS simulation and machine learning models

Nikhil Shrivastav^{*}, Jaya Madan^{*}, Rahul Pandey^{**}

VLSI Centre of Excellence, Chitkara University Institute of Engineering and Technology, Chitkara University, Punjab, India



ARTICLE INFO

Communicated by Asgari Reza

Keywords:

Metal halide perovskite
Simulations
Solar cell
Machine learning
Photovoltaic

ABSTRACT

Conventional perovskite-based solar cells (PSCs) have emerged as promising candidates for next-generation solar energy due to their remarkable features, including a high absorption coefficient, tunable bandgaps, high mobility, low maintenance cost, and high power conversion efficiency (PCE). However, the major bottleneck in commercialization of conventional PSCs is their poor stability (of few days), and toxicity concerns (due to lead content). To address these challenges cesium-based perovskites are widely adopted by researchers. However, detailed understanding of these devices considering several device parameters and their connection with overall PCE is not comprehensively disclosed in previous findings. Therefore, in this study, the PV performance of six (6) different PSCs with Cs-based absorber layer (CAL) viz. CsPbI_3 , CsPbBr_3 , CsSnCl_3 , CsSnI_3 , $\text{Cs}_2\text{AgBiBr}_6$ and $\text{CsSn}_{0.5}\text{Ge}_{0.5}\text{I}_3$ has been investigated through SCAPS simulator, followed by developing few machine learning models to forecast the efficiency. Total 2160 dataset has been obtained by varying the absorber layer, thickness, and doping and defect density for training and testing the five different machine learning algorithms such as linear regression (LR), support vector regression (SVR), neural network (NN), random forest (RF), and XGBoost (XGB). The XGB algorithm outperforms other approaches, achieving an impressive R^2 of 99.99 % and low MSE of 0.0006. Impact of each input variable on the efficiency is also obtained by generating SHAP plot for each model which revealed that absorber layer and its thickness variation greatly affected the PCE and least impact of doping is observed on PCE. Among all the absorbers, CsPbI_3 shows promising performance by delivering a maximum PCE of 14.00 %. Results reported in this work along with developed ML models may pave the way in the development of Cs based PSCs without the need of complex device simulations.

1. Introduction

Perovskite solar cells (PSC) have gained significant attention in recent years due to their high power conversion efficiency (PCE), tunable bandgaps, and low-cost manufacturing processes [1–4]. Dong et al. highlighted the crucial contribution of Metal Halide Perovskites (MHPs) in advancing modern optoelectronics. This insight was anticipated to fuel innovative research avenues in the field of MHPs and accelerated their diverse applications in the next era of optoelectronics [5,6]. The study done by Chu et al. outlined future prospects, emphasizing the need for high-quality perovskite films in large-area photovoltaic modules [7]. These PSC typically consist of a perovskite absorber layer sandwiched between electron (ETL) and hole transport layers

(HTL) [8–10]. The properties of the absorber layer play a crucial role in determining the device's overall performance [11,12]. Extensive research has been conducted to identify the best perovskite materials for the absorber layer, and several candidates have emerged as promising contenders, such as CsPbI_3 , CsPbBr_3 , CsSnCl_3 , CsSnI_3 and $\text{Cs}_2\text{AgBiBr}_6$, as shown in Fig. 1(a–e). CsPbI_3 and CsPbBr_3 perovskites have demonstrated impressive efficiencies and stability, with CsPbI_3 particularly excelling in terms of PCE [13]. Ren et al. achieved a record efficiency of 18.75 % in a CsPbI_3 -based cell by using a HTL based on P3HT and incorporating the nematic liquid crystal molecule 4-Cyano-4-Pentylbiphenyl (5CB), resulting in enhanced hole mobility and improved energy level matching, leading to the impressive efficiency [14]. Ten et al. introduced a novel approach involving a low-temperature

* Corresponding author.

** Corresponding author.

E-mail addresses: jaya.madan@chitkara.edu.in (J. Madan), rahul.pandey@chitkara.edu.in (R. Pandey).

post-treatment of quaternary bromide salts to create an interfacial gradient heterostructure, achieving highly efficient CsPbI_3 PSC with an exceptional efficiency of 21.31 % and an extraordinary fill factor of 85.40 % [15].

In terms of bandgap tunability and stability, CsPbBr_3 has shown superiority over CsPbI_3 in PSC [16–18]. However, CsPbI_3 exhibits excellent performance and thermal stability but is limited by its sensitivity to moisture. To address this, researchers introduced CsPbBr_3 pieces onto the TiO_2 ETL before depositing the CsPbI_3 film. These CsPbBr_3 pieces act as nucleation seeds, aiding in the crystal growth of CsPbI_3 and reducing trap defects in the material [16].

To address concerns about lead toxicity, research has been focused on developing lead-free perovskite materials for more environmentally friendly solar cell applications. Several lead-free metal halide perovskite materials, such as CsSnCl_3 and CsSnI_3 , have been proposed as active layers in various PSC, exhibiting excellent moisture stability and tunable bandgaps [19,20]. In a recent study, researchers enhanced the structural, electronic, and optical properties of CsSnCl_3 perovskite nanomaterial by incorporating reduced graphene oxide to improve solar cell applications [21].

Now, researchers have shifted their trend towards double perovskite materials like $\text{Cs}_2\text{AgBiBr}_6$: Cesium Silver Bismuth Bromide, $\text{Ba}_2\text{MgTeO}_6$: Barium Magnesium Tellurium Oxide, $\text{Sr}_2\text{FeMoO}_6$: Strontium Iron Molybdenum Oxide, $\text{Ca}_2\text{FeReO}_6$: Calcium Iron Rhenium Oxide, $\text{Na}_2\text{MnSbO}_6$: Sodium Manganese Antimony Oxide $\text{Cs}_2\text{BiAgI}_6$, [22–24]. Lead-free halide double perovskites (HDPs) with the chemical formula $\text{A}_2\text{B}^{+}\text{B}^{3+}\text{X}_6$ are emerging as promising alternatives to address the toxicity concerns associated with lead-based halide perovskites (APbX_3) [25]. HDPs exhibit excellent stability, a broad range of potential compositions, and appealing optoelectronic properties. Despite extensive research on novel HDPs, the PCE of state-of-the-art double PSC still lags behind that of dominant lead-based ones [22,26]. $\text{Cs}_2\text{AgBiBr}_6$ perovskite has shown great potential as a lead-free alternative with high stability and suitable bandgap. The $\text{Cs}_2\text{AgBiBr}_6$ double perovskite, formed by replacing two Pb^{2+} ions in the crystal lattice with Ag^+ and Bi^{3+} , has piqued the interest of researchers due to its easily adaptable chemical compositions [27,28]. The impact of alternative coating processes, namely vacuum sublimation and solution processing, on the optoelectronic characteristics and photovoltaic performance of $\text{Cs}_2\text{AgBiBr}_6$ thin

films was investigated by Igbari et al. [28]. Further, the significant valence band offset between $\text{Cs}_2\text{AgBiBr}_6$ and the hole transport layer (HTL) limited the efficiency of PSCs. To address this, novel deep-level hole transport materials were developed, which reduced the offset but imposed limits. A gradient energy level arrangement was devised to improve efficiency, integrating deep-level HTM TF with Spiro-OMeTAD, yielding an excellent 3.50 % PCE with high open-circuit voltage and fill factor in $\text{Cs}_2\text{AgBiBr}_6$ PSCs [29].

In this context, Chen et al. demonstrate the use of the lead-free, all-inorganic cesium tin-germanium triiodide ($\text{CsSn}_{0.5}\text{Ge}_{0.5}\text{I}_3$) solid-solution perovskite as the light absorber in PSCs, delivering promising efficiency of up to 7.11 % [30].

In addition to its already profound impact on various domains, machine learning (ML) has emerged as an influential tool for analyzing and optimizing intricate systems [32–34]. Through the implementation of ML algorithms, copious amounts of simulated data can be processed and analyzed to unveil trends, correlations, and eventually optimize material properties [35,36]. This approach has demonstrated great success in expediting the discovery and design of novel materials across diverse fields.

In this study, ML is implemented to avoid the tedious and time-consuming calculations that are generally required in simulations. SCAPS 1 d generates a large dataset of 2160 samples through modifying the thickness, bulk defect density (BDD), and doping of six different active layers. Following that, a variety of ML methods are used to forecast the optimal PCE based on the dataset, including linear regression (LR), support vector regression (SVR), neural network (NN), random forest (RF), and XGBoost (XGB). This combination of ML and material science has the potential to revolutionise the optimization process and accelerate the development of cutting-edge materials.

2. Simulation methodology and cell structures

The study compares the performance of different perovskite materials without disruption from changes in the charge transport layers by employing the identical ETL (PCBM-C₆₀) and HTL (Spiro-OMeTAD) for all six absorber materials. The schematic of the PSC under consideration has been shown in Fig. 2, where the Cs-based perovskite absorber layers (CAL) are CsPbI_3 , CsPbBr_3 , CsSnCl_3 , CsSnI_3 , $\text{CsSn}_{0.5}\text{Ge}_{0.5}\text{I}_3$ and

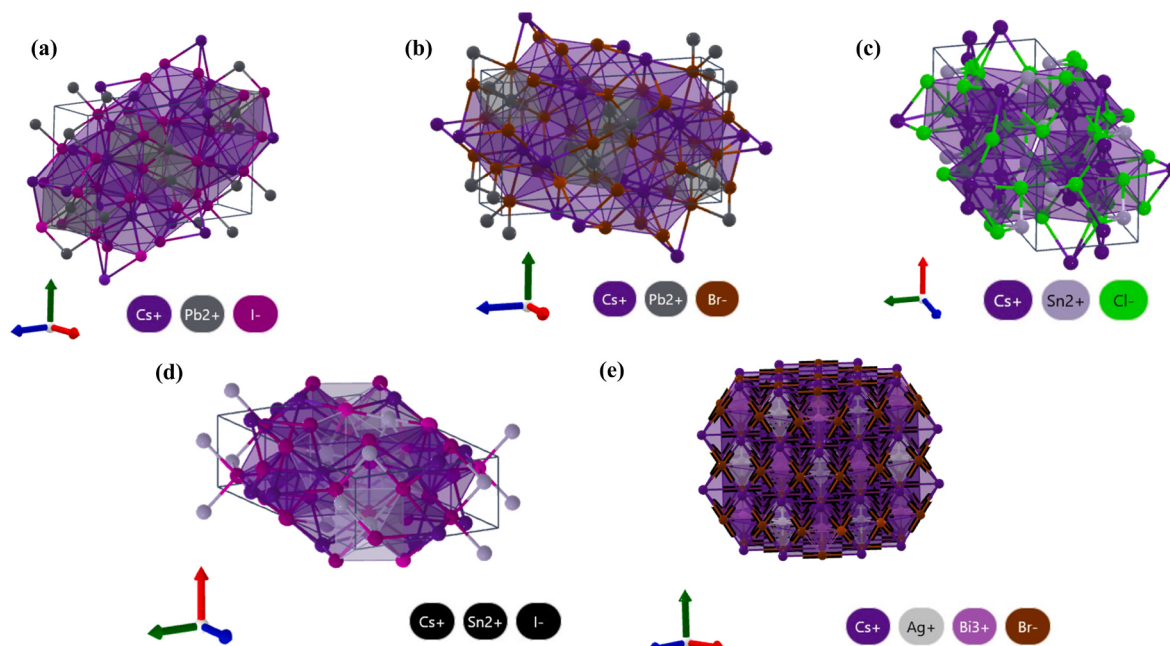


Fig. 1. Crystal structure of Cs-based perovskite materials [31]. (Reprinted under Creative Commons Attribution 4.0 License).

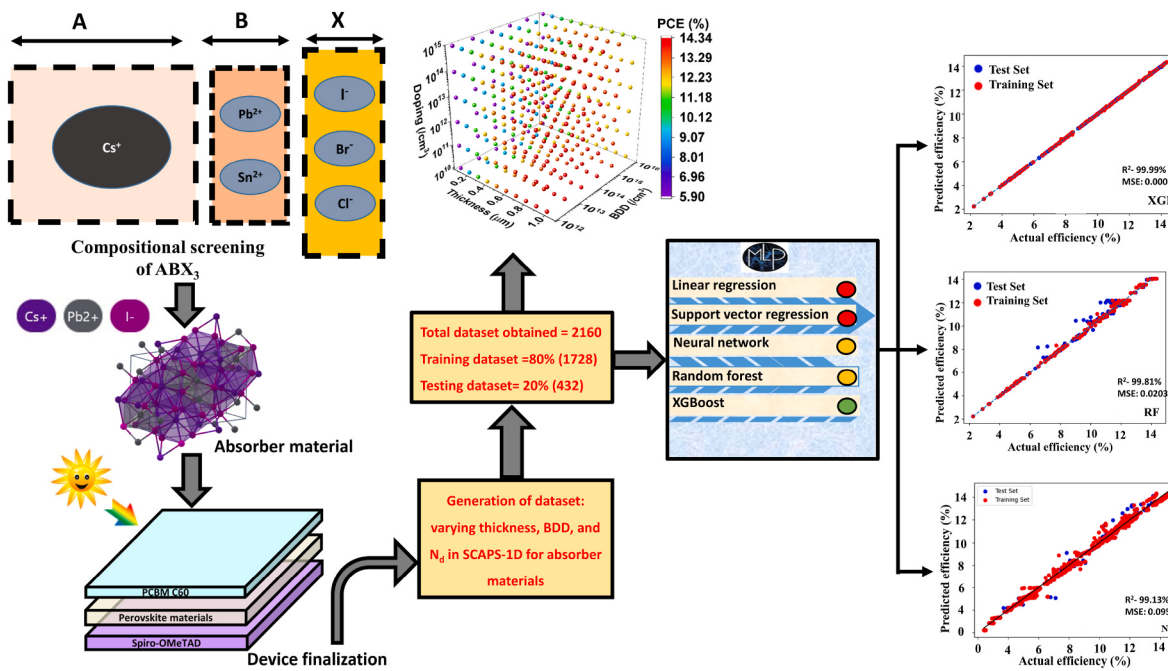


Fig. 2. PSC structure and process flow diagram.

$\text{Cs}_2\text{AgBiBr}_6$. Precisely, these six CALs are tested alternately with 80 nm thick PCBM-C₆₀ ETL and a 20 nm thick Spiro-OMeTAD HTL.

PCBM-C₆₀ facilitates the efficient extraction and transport of electrons towards cathode. While Spiro-OMeTAD allows efficient hole movement, complementing the function of the ETL, assisting efficient hole collection. Six PSCs have been studied through thickness, BDD and doping of the six CAL by utilizing SCAPS 1D software. Further, the thickness of the CAL is systematically varied, ranging from 0.1 to 1 μm . The BDD is observed across six steps, covering BDD from 1×10^{12} to $1 \times 10^{16}/\text{cm}^3$. Additionally, the doping concentration is varied from 1×10^{10} to $1 \times 10^{15}/\text{cm}^3$ to achieve the best PCE for all six PSCs. These variations are applied to six different PSCs in a cumulative manner. Upon obtaining the results from the simulator, a dataset comprising 2160 entries have been obtained. To enhance accuracy and save computation time, various ML algorithms are employed, avoiding the complexities involved in direct simulator calculations. Specifically, 1728 datasets are utilized for training the ML models, while the remaining 432 datasets are used for testing the data's predictive performance. The PSC structure and working methodology is clearly depicted in Fig. 2.

3. Results and discussion

SCAPS 1D simulator has been used for data collecting and simulating in the present study. The optimization of six different CAL in terms of their thickness (0.1–1 μm), BDD (1×10^{12} to $1 \times 10^{16}/\text{cm}^3$), and doping (1×10^{10} to $1 \times 10^{15}/\text{cm}^3$) have been done in Section 3.1. Following that, in section 3.2, several ML algorithms have been used to predict the best PCE for all cells based on the acquired data from the simulator.

3.1. Cumulative impact of the variation in thickness, BDD and doping on the six different chosen PSC

The objective is to optimize the characteristics of these PSC for better PV performance. To achieve this, cumulative variations in three key parameters have been explored: (0.1–1 μm), BDD (1×10^{12} to $1 \times 10^{16}/\text{cm}^3$), and doping (1×10^{10} to $1 \times 10^{15}/\text{cm}^3$) for each of the six different CAL. Through a series of simulations and observations, it has been obtained that the CsPbI_3 -based cell exhibited superior performance

compared to the other chosen CALs. Fig. 3(a) illustrates the clear trend, indicating that the best PCE is achieved with the CsPbI_3 -based cell, reaching a maximum PCE of 14.00 %. This high PCE is achieved with optimized conditions of 0.8 μm thickness, $1 \times 10^{12}/\text{cm}^3$ BDD, and $1 \times 10^{12}/\text{cm}^3$ intentional doping (N_d). Due to concerns regarding the toxicity of lead content in CsPbI_3 , the study has been extended its focus to explore lead-free alternatives, such as CsSnCl_3 , CsSnI_3 , $\text{CsSn}_{0.5}\text{Ge}_{0.5}\text{I}_3$ and $\text{Cs}_2\text{AgBiBr}_6$. The electrical properties of all the CAL, PCBM-C₆₀ and Spiro-OMeTAD have been tabulated in Table 1. Variations in thickness, BDD, and doping for these lead-free materials have been analyzed, and the results have been plotted in Fig. 3(c–f).

Table 2 summarises and provides the results of all simulations, including the optimized thickness, BDD, and N_d for every perovskite material based PSC. Increased perovskite layer thickness allows for higher photons absorption, reduced BDD improves charge carrier mobility, and optimized doping (N_d) improves the charge transport characteristics of PSC. The aforementioned properties are combined responsible for improving the performance and PCE of PSCs. However, finding an optimized thickness and N_d is critical, since excessively thick layers or doping can potentially cause to performance degradation and other difficulties. The results presented here provide an in-depth look at the performance of the several perovskite-based cells under investigation. The study includes the corresponding external quantum efficiency (EQE) and current-voltage (JV) curves for all the cells shown in Fig. 4 (a–b).

3.2. Predicting PCE of different chosen PSC: a ML approach with diverse algorithms

The procedure of using simulators to predict the PCE of the six selected perovskite material-based PSC is tedious, requires significant effort, and involves extensive computations. However, in order to solve the limitations of the simulator, the study has moved its attention to ML technique. The work tries to solve the problems associated with simulators by leveraging the capabilities of ML algorithms. First, the dataset has been created by computational modelling variations in thickness, BDD, and N_d by using the SCAPS 1D simulator. A total of 2160 datasets have been generated and utilized to prepare inputs for the ML algorithm. Among these datasets, 80 % (1728) are selected for training purposes,

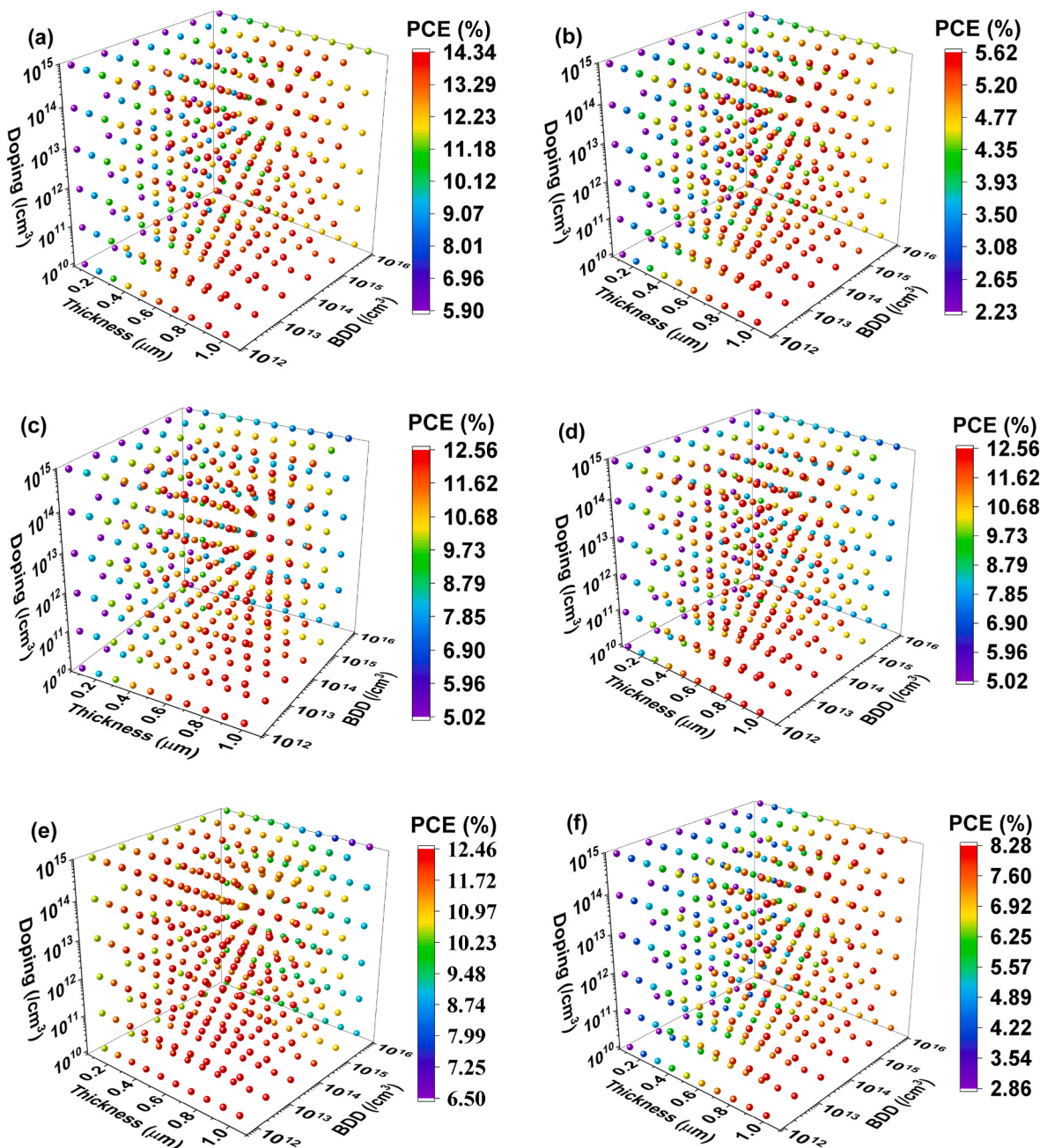


Fig. 3. Impact of the cumulative variation in thickness, BDD and N_d on (a) CsPbI₃ (b) CsPbBr₃ (c) CsSnCl₃, (d) CsSnI₃ (e) CsSn_{0.5}Ge_{0.5}I₃ and (f) Cs₂AgBiBr₆ - based PSCs.

Table 1

Details of various electrical parameters of the layers utilized during simulations [1,13,30,37–40].

| Properties | CsPbI ₃ | CsPbBr ₃ | CsSnCl ₃ | CsSnI ₃ | CsSn _{0.5} Ge _{0.5} I ₃ | Cs ₂ AgBiBr ₆ | Spiro OMeTAD | PCBM |
|---|--------------------|---------------------|----------------------|--------------------|--|-------------------------------------|----------------------|----------------------|
| Bandgap (eV) | 1.73 | 2.30 | 1.52 | 1.30 | 1.50 | 2.05 | 3.00 | 1.70 |
| Electron affinity | 3.95 | 3.40 | 3.90 | 3.28 | 3.90 | 4.19 | 2.40 | 4.50 |
| Dielectric constant | 10.00 | 10.00 | 29.40 | 48.20 | 6.50 | 5.8 | 3.00 | 6.00 |
| CB effective density (cm^3) | 1×10^{20} | 1×10^{20} | 1.1×10^{20} | 1×10^{19} | 1×10^{18} | 1×10^{19} | 2.2×10^{18} | 1×10^{19} |
| VB effective density (cm^3) | 8×10^{19} | 8×10^{19} | 8×10^{19} | 1×10^{18} | 1×10^{19} | 1×10^{19} | 1.8×10^{19} | 1×10^{19} |
| Electron mobility (cm^2/Vs) | 1.6×10^1 | 1.6×10^1 | 2×10^0 | 5×10^1 | 1.6×10^{-1} | 5×10^{-1} | 1×10^{-4} | 1.6×10^{-3} |
| Hole mobility (cm^2/Vs) | 1.6×10^1 | 1.6×10^1 | 2×10^0 | 4×10^2 | 1.6×10^{-1} | 1×10^{-1} | 1×10^{-4} | 1.6×10^{-3} |
| N_D (cm^{-3}) | 1×10^{15} | 1×10^{15} | 1×10^{15} | 1×10^{15} | 1×10^{15} | 1×10^{16} | 0 | 1.8×10^{17} |
| N_A (cm^{-3}) | 1×10^{15} | 1×10^{15} | 1×10^{15} | 1×10^{15} | 1×10^{15} | 1×10^{16} | 3×10^{18} | 0 |

Table 2

Different PV parameters obtained from the simulator at optimized thickness, BDD and N_d .

| Absorber materials | Optimized Thickness (μm) | Observed BDD ($/\text{cm}^3$) | Optimized N_d ($/\text{cm}^3$) | PCE (%) | V_{OC} (V) | J_{SC} (mA/cm^2) | FF (%) |
|-------------------------------------|---------------------------------------|---------------------------------|------------------------------------|---------|--------------|--------------------------------------|--------|
| CsPbI ₃ | 0.8 | 1×10^{12} | 1×10^{12} | 14.00 | 0.861 | 19.37 | 83.91 |
| CsPbBr ₃ | 0.6 | 6.31×10^{12} | 1×10^{15} | 5.13 | 0.851 | 7.13 | 84.60 |
| CsSnCl ₃ | 0.8 | 3.98×10^{12} | 1×10^{12} | 12.28 | 0.632 | 25.87 | 75.02 |
| CsSnI ₃ | 0.5 | 6.31×10^{12} | 1×10^{15} | 11.67 | 0.633 | 24.10 | 76.50 |
| CsSn ₃ Ge _{0.5} | 0.3 | 6.31×10^{12} | 1×10^{10} | 12.01 | 0.712 | 21.14 | 79.72 |
| Cs ₂ AgBiBr ₆ | 1.0 | 1×10^{13} | 1×10^{15} | 7.45 | 0.967 | 10.03 | 76.79 |

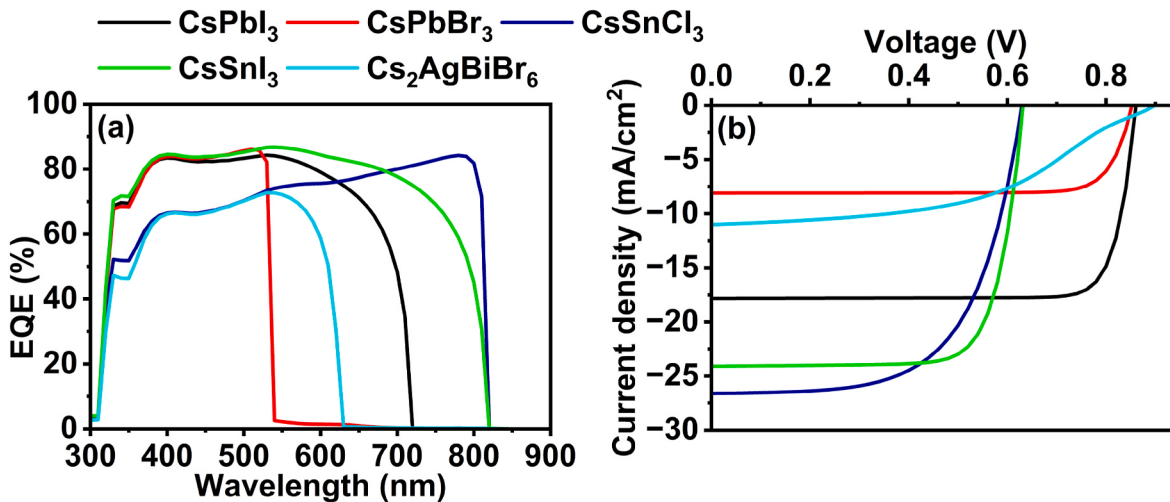


Fig. 4. Optimized (a) EQE (b) J-V curves of each Cs-based PSC.

while the remaining 20 % (300) are reserved for testing. Further, python code is used to project PCE, using linear regression (LR) and support vector regression (SVR) approaches. However, the results are not as optimistic as anticipated. Both LR and SVR had high mean squared error (MSE_{LR} - 4.955 and MSE_{SVR} - 11.634) values, indicating a significant difference between predicted and actual values. Furthermore, the R-squared values (54.11 % for LR and 5.86 % for SVR), which show the models' goodness-of-fit, are disappointingly low for both approaches. The equation which is used for the MSE and R^2 calculations [41] are given below:

$$MSE = \frac{1}{n} \sum_{i=1}^n \left(y_i - \hat{y}_i \right)^2 \quad (1)$$

$$R^2 = 1 - \sum_{i=1}^n \frac{\left(y_i - \hat{y}_i \right)^2}{\sum_{i=1}^n \left(y_i - \bar{y} \right)^2} \quad (2)$$

Where, y_i is the actual value, \hat{y} is the predicted values, \bar{y} is the mean of the actual values and n is the total no. Of datasets.

The same dataset has been then used to test a total of three approaches for better prediction of PCE for the different chosen perovskite based cells: NN, RF, and XGB. Fig. 5(a-f) shows obtained plots such as SHAP and actual vs predicted PCE curves from all aforementioned ML algorithms. The code begins by importing the essential libraries after applying the NN for PCE prediction. These libraries are used to read data from a CSV file and organise it into a pandas data frame.

The data frame is subsequently separated into features (CALs, thickness, BDD, and N_d) and the target variable (PCE). The code then defines a model-building method that makes use of Keras Tuner. The Keras Tuner is started, and early termination is enabled to optimize hyperparameter tuning performance. The Keras Tuner is then used to fine-tune the model's hyperparameters. After identifying the optimum

hyperparameters, the model is built with those values and trained on the training dataset. The code predicts the target variable (PCE) on the test dataset using the trained model. After identifying the optimum hyperparameters, the model is built with the appropriate values and trained on the training dataset. The code predicts the target variable (PCE) on the test dataset using the trained model. R^2 (Coefficient of Determination) and MSE (Mean Squared Error) scores are quite satisfactory, with R^2 reaching an astounding 99.13 % and MSE at a promising 0.0095. Additionally, the code generates a SHAP plot using Python code, as depicted in Fig. 5(b).

The programme investigates an additional method known as RF to evaluate different ML algorithms for PCE prediction. To achieve accurate predictions, this ensemble learning technique integrates many decision trees. The code begins similarly to the prior way by importing relevant libraries such as scikit-learn, pandas, and numpy. The data is then read from a CSV file and separated into features (CALs, thickness, BDD, and N_d) and the target variable (PCE).

To compare different ML techniques for PCE prediction, the code explores another algorithm known as RF. This ensemble learning technique combines multiple decision trees to achieve accurate predictions. Similar to the previous approach, the code begins by importing necessary libraries, such as scikit-learn, pandas, and numpy. The data is then read from a CSV file and separated into features (CALs, thickness, BDD, and N_d) and the target variable (PCE). A RF regressor model is trained using the collected data. To evaluate the model's predictions, the method additionally constructs a SHAP plot in Python (Fig. 5(d)). This algorithm's output is highly promising, surpassing the NN with an R^2 of 99.81 % and an MSE of 0.0203.

While both the NN and the RF algorithms produced acceptable results, the code investigates the XGB technique to see if it may enhance PCE prediction for the selected perovskite-based cells. It uses a similar method, importing the necessary libraries and reading data from a CSV file. After that, the data is separated into features (CALs, thickness, BDD,

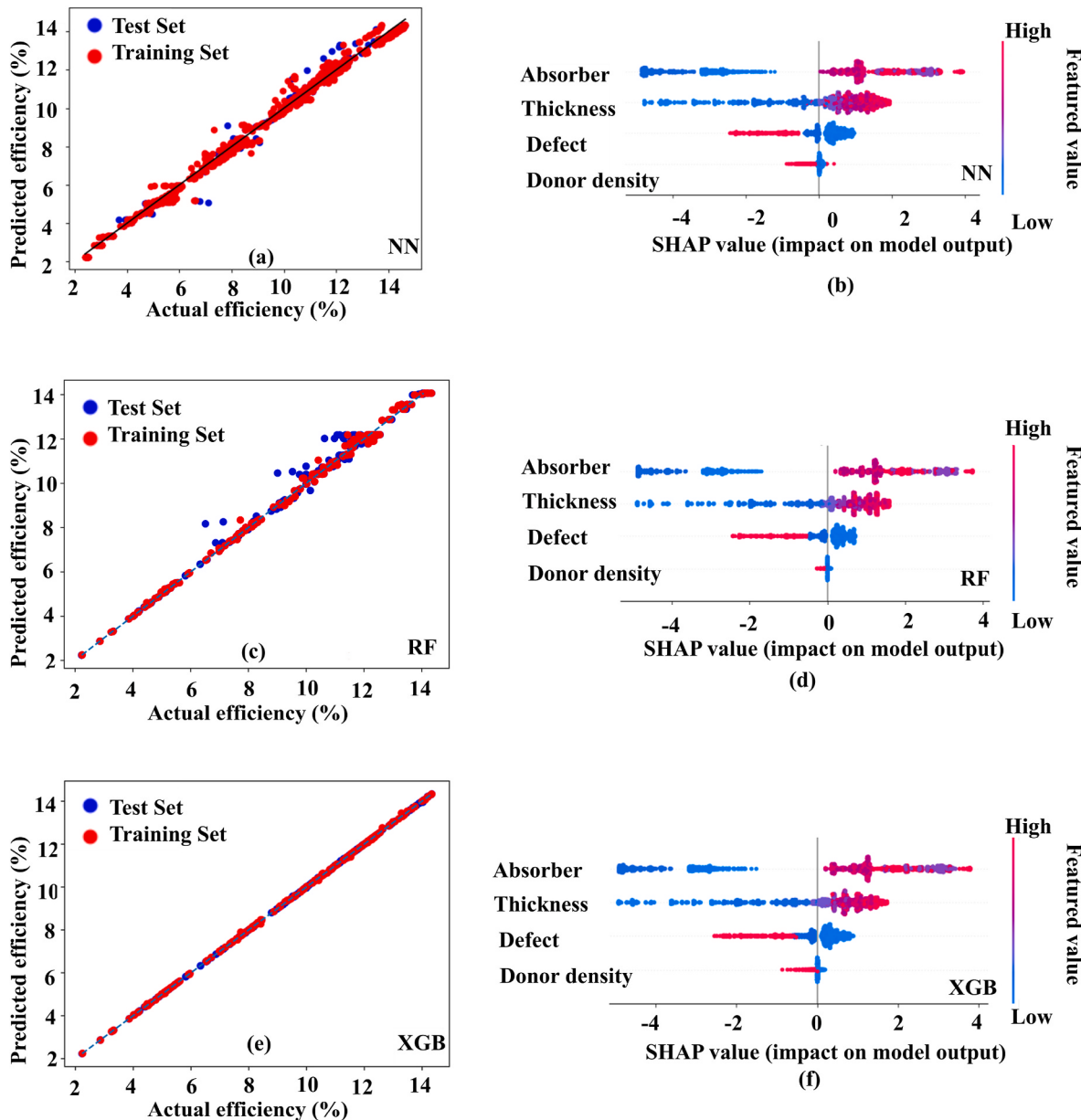


Fig. 5. Scattered plots for actual PCE vs predicted PCE of (a) neural network (c) Random forest and (e) XGBoost. (b, d and f) SHAP plot for three algorithms.

and N_d) and the target variable (PCE). Following that, an XGB Regressor model is built, and hyperparameters such as learning rate and tree depth limit are selected, which have a substantial impact on the model's performance. The code performs a Grid Search CV to discover the optimal hyperparameters, which trains the model on multiple hyperparameter combinations and evaluates its performance on a holdout dataset.

The algorithm constructs the ultimate XGB Regressor model after determining the optimum hyperparameters. It tests the model on the test set after training on the training set to determine its prediction capabilities. The XGB method outperforms all prior algorithms, with an amazing R^2 of 99.99 % and a very low MSE of 0.0006. In conclusion, based on the high R-squared value and the low MSE, it is evident that the XGB algorithm yields the most accurate PCE predictions among all the algorithms applied in this study.

Fig. 6(a-d) illustrates the behaviour of the PCE in perovskite-based cells concerning different factors, including absorber materials, thickness, BDD, and N_d . Fig. 6(b) indicates that the PCE tends to increase with an increasing absorber layer thickness up to a certain point, beyond which it starts to decrease. This trend can be attributed to the thicker

absorber layer's enhanced sunlight absorption capability, but it also hinders the smooth flow of charge carriers through the layer. On the other hand, Fig. 6(c-d) demonstrates that the PCE decreases as the BDD and N_d increase. This is due to defects and donor atoms acting as recombination centres, leading to the trapping of charge carriers and inhibiting their contribution to the overall current.

4. Conclusion

Six Cs-based PSC are comprehensively investigated by varying the thickness, BDD and doping concentration using SCAPS-1D. A complete dataset of 2160 has been obtained for the above-mentioned changes to develop the supervised ML models using five different algorithms such as LR, SVR, NN, RF and XGB. The ML approaches are adopted in the study to build a model that can forecast the PCE without the need to complex device simulators for the devices under consideration. The XGB, RF and NN perform well with R^2 and MSE of 99.99 % and 0.0006, 99.81 % and 0.0203, 99.13 % and 0.0095, respectively. A thorough set of computations and measurements revealed that the CsPbI₃-based PSC

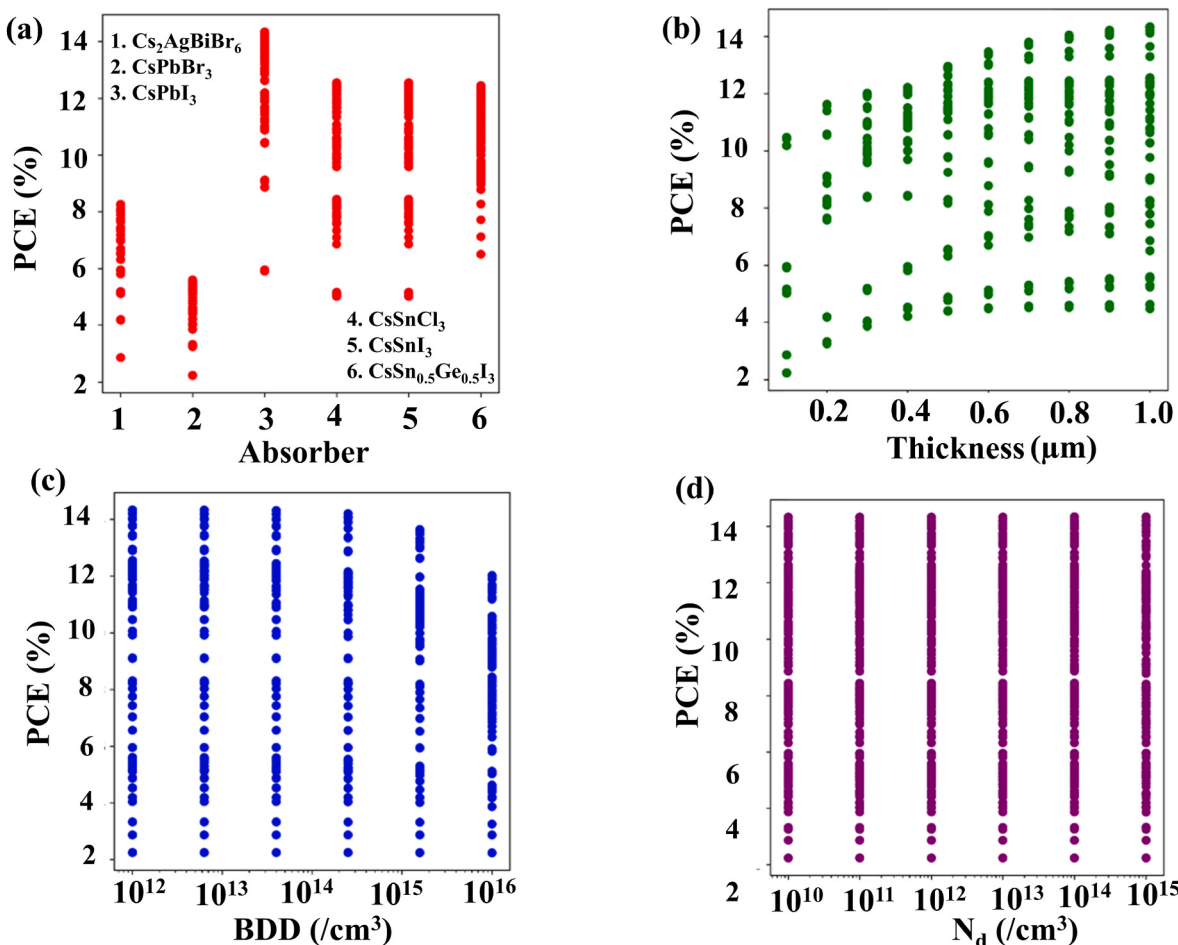


Fig. 6. Impact in PCE after the variation in (a) absorber materials (b) thickness of active layers (c) BDD and (d) N_d.

performed better than the other perovskite materials. The CsPbI₃-based cell attained an excellent maximum PCE of 14.00 % under optimized circumstances of 0.8 μm thickness, 1 × 10¹²/cm³ BDD, and 1 × 10¹²/cm³ doping (N_d). Combined SCAPS-1D and ML strategy adopted in this work can further be extended to other materials and devices in future.

CRediT authorship contribution statement

Nikhil Shrivastav: Data curation, Formal analysis, Methodology, Writing – original draft. **Jaya Madan:** Formal analysis, Supervision, Writing – review & editing. **Rahul Pandey:** Formal analysis, Investigation, Supervision, Writing – review & editing.

Declaration of competing interest

The authors declare that they have no known competing financial interests or personal relationships that could have appeared to influence the work reported in this paper.

Data availability

Data will be made available on request.

Acknowledgment

For all the support in this research work, the authors are very thankful to the VLSI Centre of Excellence, Chitkara University, Punjab, India.

Appendix A. Supplementary data

Supplementary data to this article can be found online at <https://doi.org/10.1016/j.ssc.2024.115437>.

References

- [1] A. Al-Ashouri, et al., Monolithic perovskite/silicon tandem solar cell with > 29% efficiency by enhanced hole extraction, *Science* 370 (6522) (2020) 1300–1309.
- [2] C. Bao, et al., High performance and stable all-inorganic metal halide perovskite-based photodetectors for optical communication applications, *Adv. Mater.* 30 (38) (2018) 1803422.
- [3] R.K. Kothandaraman, Y. Jiang, T. Feurer, A.N. Tiwari, F. Fu, Near-infrared-transparent perovskite solar cells and perovskite-based tandem photovoltaics, *Small Methods* 4 (10) (2020) 2000395.
- [4] M. He, D. Zheng, M. Wang, C. Lin, Z. Lin, High efficiency perovskite solar cells: from complex nanostructure to planar heterojunction, *J. Mater. Chem. A* 2 (17) (2014) 5994–6003.
- [5] H. Dong, C. Ran, W. Gao, M. Li, Y. Xia, W. Huang, Metal Halide Perovskite for next-generation optoelectronics: progresses and prospects, *ELight* 3 (1) (2023) 3.
- [6] T. Dureja, A. Garg, S. Bhalla, D. Bhutani, A. Khanna, Double lead-free perovskite solar cell for 19.9% conversion efficiency: a SCAPS-1D based simulation study, *Mater. Today Proc.* 71 (2022) 239–242.
- [7] L. Chu, et al., High-performance large-area perovskite photovoltaic modules, *Nano Research Energy* 1 (2) (2022) e9120024.
- [8] C. Momblona, et al., Efficient vacuum deposited pin and nip perovskite solar cells employing doped charge transport layers, *Energy Environ. Sci.* 9 (11) (2016) 3456–3463.
- [9] G. Yang, H. Tao, P. Qin, W. Ke, G. Fang, Recent progress in electron transport layers for efficient perovskite solar cells, *J. Mater. Chem. A* 4 (11) (2016) 3970–3990.
- [10] N. Shrivastav, S. Kashyap, J. Madan, M.K. Mohammed, M.K. Hossain, R. Pandey, An efficient all-perovskite two terminal monolithic tandem solar cell with improved photovoltaic parameters: a theoretical prospect, *Optik* 281 (2023) 170821.

- [11] N. Shrivastav, J. Madan, R. Pandey, A.E. Shalan, Investigations aimed at producing 33% efficient perovskite-silicon tandem solar cells through device simulations, *RSC Adv.* 11 (59) (2021) 37366–37374.
- [12] A.R. Dogra, P. Kumar, V. Sharma, P. Malik, P. Khanra, M. Kapoor, Deposition of nanoparticles layer on ITO substrate and its application for alignment control of liquid crystal, in: *AIP Conference Proceedings*, vol. 2357, AIP Publishing LLC, 2022 050019, 1.
- [13] N. Shrivastav, J. Madan, M. Ka Mohammed, M.K. Hossain, R. Pandey, CsPbI_3 -Perovskite quantum dot solar cells: unlocking their potential through improved absorber layer characteristics and reduced defects, *Mater. Res. Express* 10 (7) (2023) 075506 (2023).
- [14] W. Ren, et al., Cyano-4'-Pentylbiphenyl dopant strategy for P3HT-Based CsPbI_3 perovskite solar cells with a record efficiency and preeminent stability, *Chem. Eng. J.* 455 (2023) 140831.
- [15] S. Tan, et al., Constructing interfacial gradient heterostructure enables efficient CsPbI_3 perovskite solar cells and printed minimodules, *Adv. Mater.* (2023) 2301879.
- [16] W. Chai, et al., CsPbBr_3 seeds improve crystallization and energy level alignment for highly efficient CsPbI_3 perovskite solar cells, *Chem. Eng. J.* 452 (2023) 139292.
- [17] M.J. Patel, S.K. Gupta, P. Gajjar, Investigation of thickness dependent efficiency of CsPbX_3 ($X = \text{I}, \text{Br}$) absorber layer for perovskite solar cells, *J. Phys. Chem. Solid.* 176 (2023) 111264.
- [18] H. Yang, et al., Recent progress of film fabrication process for carbon-based all-inorganic perovskite solar cells, *Crystals* 13 (4) (2023) 679.
- [19] M.K. Hossain, et al., Deep Insights into the Coupled Optoelectronic and Photovoltaic Analysis of Lead-Free CsSnI_3 Perovskite-Based Solar Cell Using DFT Calculations and SCAPS-1D Simulations, *ACS Omega*, 2023.
- [20] Q. Fatima, A.A. Haidry, R. Hussain, H. Zhang, Device simulation of a thin-layer CsSnI_3 -based solar cell with enhanced 31.09% efficiency, *Energy Fuels* 37 (10) (2023) 7411–7423.
- [21] A. Kumar, N. Pandey, D. Punetha, R. Saha, S. Chakrabarti, Tenability and improvement of the structural, electronic, and optical properties of lead-free CsSnCl_3 perovskite by incorporating reduced graphene oxide (rGO) for optoelectronic applications, *J. Mater. Chem. C* 11 (10) (2023) 3606–3615.
- [22] X. Yang, W. Wang, R. Ran, W. Zhou, Z. Shao, Recent advances in $\text{Cs}_2\text{AgBiBr}_6$ -based halide double perovskites as lead-free and inorganic light absorbers for perovskite solar cells, *Energy Fuels* 34 (9) (2020) 10513–10528.
- [23] M.K. Hossain, et al., Design and simulation of $\text{Cs}_2\text{AgBiBr}_6$ double perovskite solar cells with different electron transport layers for efficiency enhancement, *Energy Fuels* 37 (5) (2023) 3957–3979.
- [24] T.I. Alanazi, Design and device numerical analysis of lead-free $\text{Cs}_2\text{AgBiBr}_6$ double perovskite solar cell, *Crystals* 13 (2) (2023) 267.
- [25] F. Ji, G. Boschloo, F. Wang, F. Gao, Challenges and progress in lead-free halide double perovskite solar cells, *Sol. RRL* 7 (6) (2023) 2201112.
- [26] R. Marin, D. Jaque, Doping lanthanide ions in colloidal semiconductor nanocrystals for brighter photoluminescence, *Chem. Rev.* 121 (3) (2020) 1425–1462.
- [27] D. Zhao, et al., Overcoming the limitation of $\text{Cs}_2\text{AgBiBr}_6$ double perovskite solar cells through using mesoporous TiO_2 electron extraction layer, *Energy & Environmental Materials* 5 (4) (2022) 1317–1322.
- [28] F. Igbari, et al., Composition stoichiometry of $\text{Cs}_2\text{AgBiBr}_6$ films for highly efficient lead-free perovskite solar cells, *Nano Lett.* 19 (3) (2019) 2066–2073.
- [29] Z.-Y. Xia, et al., Improving performance of $\text{Cs}_2\text{AgBiBr}_6$ solar cell through constructing gradient energy level with deep-level hole transport material, *Rare Met.* 42 (9) (2023) 3004–3012.
- [30] M. Chen, et al., Highly stable and efficient all-inorganic lead-free perovskite solar cells with native-oxide passivation, *Nat. Commun.* 10 (1) (2019) 16.
- [31] A. Jain, et al., Commentary: the Materials Project: a materials genome approach to accelerating materials innovation, *Apl. Mater.* 1 (1) (2013), <https://doi.org/10.1063/1.4812323>.
- [32] V. Kukreja, P. Dhiman, A Deep Neural Network based disease detection scheme for Citrus fruits, in: *2020 International Conference on Smart Electronics and Communication (ICOSEC)*, IEEE, 2020, pp. 97–101.
- [33] Z. Liu, et al., Machine learning with knowledge constraints for process optimization of open-air perovskite solar cell manufacturing, *Joule* 6 (4) (2022) 834–849.
- [34] Y. Liu, X. Tan, J. Liang, H. Han, P. Xiang, W. Yan, Machine learning for perovskite solar cells and component materials: key technologies and prospects, *Advanced Functional Materials*, 2023 2214271.
- [35] T. Ramesh, U.K. Lilhore, M. Poongodi, S. Simaiya, A. Kaur, M. Hamdi, Predictive analysis of heart diseases with machine learning approaches, *Malays. J. Comput. Sci.* (2022) 132–148.
- [36] K. Verma, et al., *Latest Tools for Data Mining and Machine Learning*, 2019.
- [37] L. Lin, et al., Simulated development and optimized performance of CsPbI_3 based all-inorganic perovskite solar cells, *Sol. Energy* 198 (2020) 454–460.
- [38] M. Mehrabian, E.N. Afshar, S.A. Yousefzadeh, Simulating the thickness effect of the graphene oxide layer in CsPbBr_3 -based solar cells, *Mater. Res. Express* 8 (3) (2021) 035509.
- [39] M.K. Hossain, et al., An extensive study on multiple ETL and HTL layers to design and simulation of high-performance lead-free CsSnCl_3 -based perovskite solar cells, *Sci. Rep.* 13 (1) (2023) 2521.
- [40] M.T. Islam, et al., Numerical simulation studies of a fully inorganic $\text{Cs}_2\text{AgBiBr}_6$ -perovskite solar device, *Opt. Mater.* 105 (2020) 109957.
- [41] D. Chicco, M.J. Warrens, G. Jurman, The coefficient of determination R-squared is more informative than SMAPE, MAE, MAPE, MSE and RMSE in regression analysis evaluation, *PeerJ Computer Science* 7 (2021) e623.